Available online at www.sciencedirect.com

ScienceDirect

Ceramics International 37 (2011) 181–188

CERAMICS INTERNATIONAL

www.elsevier.com/locate/ceramint

Amorphous zones in flame sprayed alumina–titania–zirconia compounds

Tim Kratschmer *, Christos G. Aneziris

TU BA Freiberg, Institut für Keramik, Glas- und Baustofftechnik, Agricolastr. 17, Freiberg 09596, Germany

Received 16 July 2010; received in revised form 19 July 2010; accepted 18 August 2010

Abstract

The formation of amorphous phases in thermally sprayed coatings is a common phenomenon. This work examines the distribution of the amorphous content in flame sprayed Al_2O_3–TiO_2–ZrO_2-compounds. An amorphous percentage appears even in pure alumina and the percentage increases with increasing amount of TiO_2- and ZrO_2-addition. Amorphous sub-lamellae appear in all examined compositions. If a system with a miscibility gap in the liquid state, such as Al_2O_3–ZrO_2, is applied, the formation of secondary amorphous regions is observed. The amorphous sub-lamellae or primary amorphous region is induced only by rapid cooling, the secondary amorphous regions are induced by rapid cooling plus a spinodal demixing effect.

Keywords: Thermal spray; Amorphous; Alumina; Titania; Zirconia

1. Introduction

Rod flame spraying is used as a literally easy to handle process to study phase and microstructure evolution of coatings made from mixtures in the pseudo ternary system Al_2O_3–TiO_2–ZrO_2. The complete melt formation and mixing in liquid state is the most interesting feature of the rod flame spraying process compared to other thermal spraying techniques. This makes it suitable for homogenizing compounds with small amounts of additions or high melting points in a liquid state. The basic principles of coating build up and therefore lamellar microstructure and phase evolution are similar to for example plasma sprayed coatings. There are a high number of publications dealing with the amorphous content of thermally sprayed coatings in general, e.g. Refs. [1–11]. Amorphous regions near the coating–substrate interface are discussed in Refs. [8,12–14] and amorphous sub-lamellae in the system hydroxyapatite (HA) are presented in Refs. [15,16]. However, there is only in publications dealing with HA coatings for medical applications a clear statement concerning the distribution of amorphous sub-lamellae over the whole thickness range of the coating. This consideration emerges because the amorphous content in HA-coatings has important and direct impact on the in-vitro-performance of the coating in such a way, that the bioactivity of amorphous HA phase is much higher than that of the crystalline HA phase [6]. Finally, lots of work conducted transmission electron microscopy (TEM) examinations where sometimes amorphous phase was detected but due to the high resolution of this analyzing technique they could not be localized within the lamellae [1,17–25]. The degree of amorphization is dependent on the cooling speed. For example a cooling rate $>10^4$ K/s leads to complete amorphous phases in the eutectic system Al_2O_3–ZrO_2 [1,26–28]. In eutectic systems amorphization appears, when the velocity of the isotherms exceeds the diffusion velocity in the liquid state. From this it follows that if first, no separation of phases can take place and second, no solid phase with the melt composition exist the amorphous state is enforced upon the system [29]. It can be furthermore deduced from classical glass theory, why alumina based materials can solidify in an amorphous state. A system is as more likely to show amorphization as lower the coordination number of the cation with the oxygen is. To enable the formation of a glass network high bonding energies are required to allow bridging oxygen to appear [30,31]. The coordination number of Al^{3+} in a melt lays in the range between 4.1 and 4.4 and in gamma alumina at 4 in contrast to 6 for corundum [32,33]. The coordination number of Al^{3+} can also

---

* Corresponding author. Tel.: +49 03731392608; fax: +49 03731392419.
E-mail address: tim.kratschmer@googlemail.com (T. Kratschmer).

0272-8842/$36.00 © 2010 Elsevier Ltd and Techna Group S.r.l. All rights reserved.
doi:10.1016/j.ceramint.2010.09.020

Table 1
Examples of amorphous content in plasma sprayed materials determined with Rietveld analysis.

Material	Amorphous percentage (wt.%)	Reference
Al_2O_3	12.0 ± 0.7	[4]
Al_2O_3–13 wt.% TiO_2	50	[11]
ZrO_2–60 wt.% Al_2O_3	29	[2]

be influenced and reduced by additions, for example in the glass system $12CaO{\cdot}7Al_2O_3$ [34]. The coordination number in amorphous alumina shows a distribution with an average value of 4.5. This distribution is characterizing the amorphous state and disappears completely during crystallization [35]. In molten titania the Ti^{4+} appears in a fivefold coordination [36]. This number can also be influenced by additions, for example between 4 and 6 in a sodium silicate glass as a function of the sodia–silica ratio [34]. The Zr^{4+} in amorphous zirconia is like in monoclinic zirconia sevenfold coordinated, a similar number is assumed for the melt [37]. Hence a classical glass system with network formers and modifiers arises from the alumina–titania–zirconia ternary system under the condition of rapid cooling and by the influence of titania and zirconia additions. The amorphous content influences the mechanical properties by leading to a higher degree of adhesion between coating and substrate and between the lamellae. Higher toughness and abrasion resistance might induced by hard particles in a tough matrix or a layered amorphous and crystalline structure [11]. Three examples of the amorphous content determination in plasma sprayed materials are presented in Table 1.

2. Materials and methods

The procedure of rod and sample production is described elsewhere [38,39]. The used thermal spray apparatus is the Rokide® apparatus with a MasterJet Flame Spray Gun from SaintGobain. The ceramic raw materials were alumina CT3000SG (Almatis, Frankfurt, Germany), rutile Tronox T-R (Kerr-McGee, Oklahoma City, OK) and monoclinic zirconia (Unitec Ceramics, Stafford, UK). Phase analysis was done with a Phillips X'Pert Pro MPD diffractometer and X'Pert HighScore analysis software. The used electron microscopes were a REM FEI/Phillips Type XL 30 with EBSD detector and a TEM JEOL Type 2010 FEF. The examined mixtures with sample denotation are listed in Table 2, all values are given in weight percent. The phase compositions of the rods after sintering are summarized in Table 3 and present the trend of the equilibrium phase evolution for this system after temperature treatment at 1500 °C for 100:0:0 and 90:0:10 and at 1400 °C respectively for the remaining compositions. 20 wt.% ZnO was added as an internal standard to all samples before XRD measurement.

Table 2
Sample denotation and composition.

Sample	Al_2O_3 (wt.%)	TiO_2 (wt.%)	ZrO_2 (wt.%)
100:0:0	100	0	0
90:0:10	90	0	10
90:10:0	90	10	0
90:5:5	90	5	5
85:5:10	85	5	10
85:10:5	85	10	5
80:10:10	80	10	10

Table 3
Phase composition of rods.

Sample	Phases	Weight fraction (wt.%)	*R*-value phase (%)	*R*-value profile (%)
100:00:00	ZnO	20.0	7.85	10.42
	α-Al_2O_3	80.0	6.60	
90:00:10	ZnO	20.0	11.97	12.03
	α-Al_2O_3	71.0	9.18	
	t-ZrO_2	0.9	21.94	
	m-ZrO_2	8.1	42.00	
90:10:00	ZnO	20.0	7.65	12.27
	α-Al_2O_3	70.1	7.71	
	t-TiO_2 (rutile)	6.1	13.74	
	β-Al_2TiO_5	3.8	47.00	
90:05:05	ZnO	20.0	7.38	11.44
	α-Al_2O_3	72.0	11.12	
	t-TiO_2 (rutile)	1.2	41.00	
	$ZrTiO_4$	6.8	23.83	
85:05:10	ZnO	20.0	4.80	10.49
	α-Al_2O_3	69.7	8.27	
	m-ZrO_2	2.5	53.97	
	$ZrTiO_4$	7.8	19.66	
85:10:05	ZnO	20.0	7.79	10.70
	α-Al_2O_3	66.1	10.60	
	t-TiO2 (rutile)	3.3	28.59	
	$ZrTiO_4$	5.9	21.82	
	β-Al_2TiO_5	4.7	32.41	
80:10:10	ZnO	20.0	8.47	10.35
	α-Al_2O_3	65.3	9.42	
	t-TiO_2 (rutile)	3.0	25.10	
	$ZrTiO_4$	11.7	17.23	

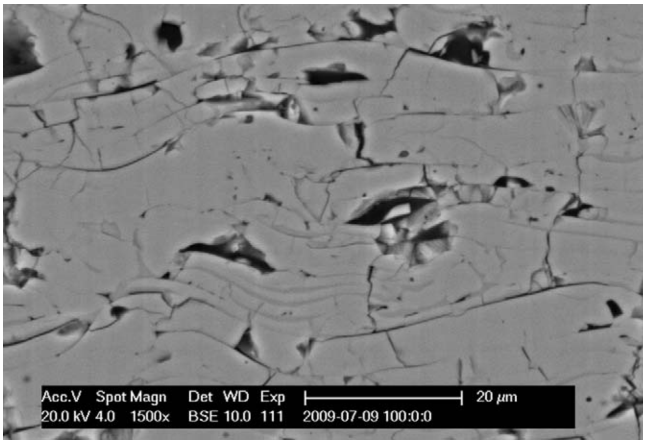

Fig. 1. Cross section of sample 100:0:0.

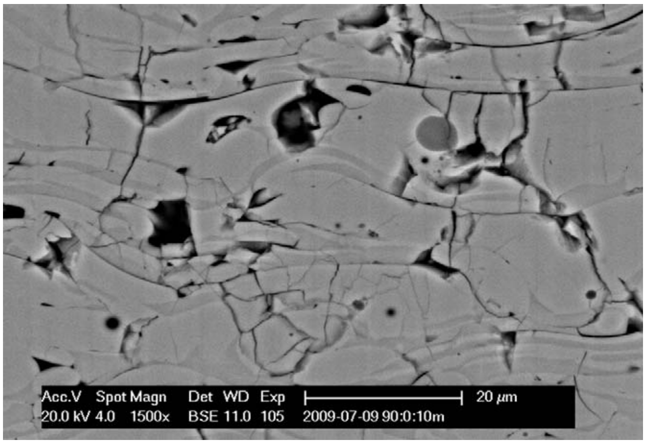

Fig. 2. Cross section of sample 90:0:10.

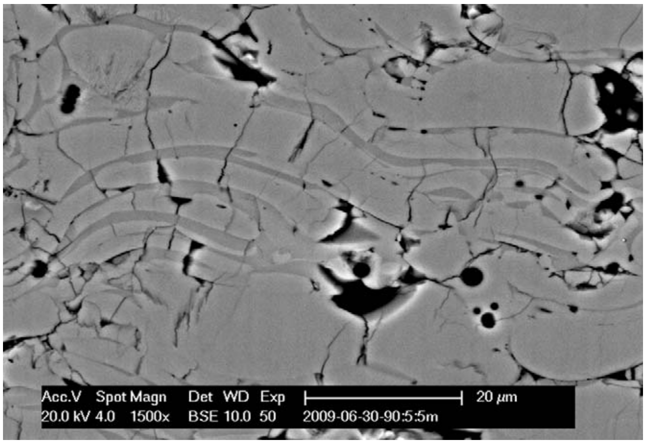

Fig. 4. Cross section of sample 90:5:5.

3. Results

3.1. Electron microscopy and electron diffraction

All compositions show a microstructure typical for thermal sprayed coatings. The presented cross sections reveal the splat morphology and microcrack patterns. The direction of deposition was perpendicular to the picture horizon with the substrate being on the bottom. Micrographs with visible amorphous sub-lamellae can be seen in Figs. 1–5. Their amorphous nature has been proofed by electron diffraction (see Fig. 5). The contrast between amorphous and crystalline regions appears both in optical (not shown) and in electron micrographs. A crack stopping effect seems to appear at the interface of lamellae–amorphous sub-lamellae.

An electron backscatter diffraction pattern (EBSP) mapping was done on the marked area shown in Fig. 5a. This mapping included three amorphous sub-lamellae and their transition to fully crystalline areas. Only 50% of the measured points could be matched with the phases gamma alumina and $Zr_5Ti_7O_{24}$ using certain fit criteria. The number of EBSPs associated with the phases gamma alumina and $Zr_5Ti_7O_{24}$ has a ratio of 2:1. The deposition direction was here parallel to the picture horizon with the substrate being at the left side. The quality distribution of the EBSP reveals three distinct areas. The first area with no analyzable diffraction pattern can be referred to the amorphous sub-lamellae visible in all micrographs. Afterwards there is an intermediate area followed by crystalline area with good diffraction pattern quality. The areas of the visible amorphous sub-lamellae were quantified using image analysis. Four images of each composition were analyzed. The error of this analysis is determined by the sharpness of the boundaries between amorphous and crystalline areas and is thus difficult to estimate. The values were specified with an accuracy of 5%-points. Due to the large aspect ratio of the lamellae of 20–40:1 the area fraction was in a first approach assumed as the volume and further as the weight fraction. The results of the area fractions are listed in Table 4. The influence of TiO_2 and ZrO_2 alone on the area seems very different to the influence of TiO_2 and ZrO_2 together. Compared to pure Al_2O_3 for all mixtures an increase occurs.

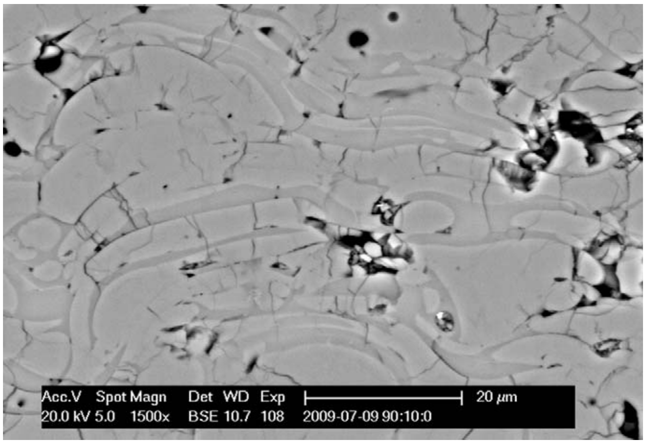

Fig. 3. Cross section of sample 90:10:0.

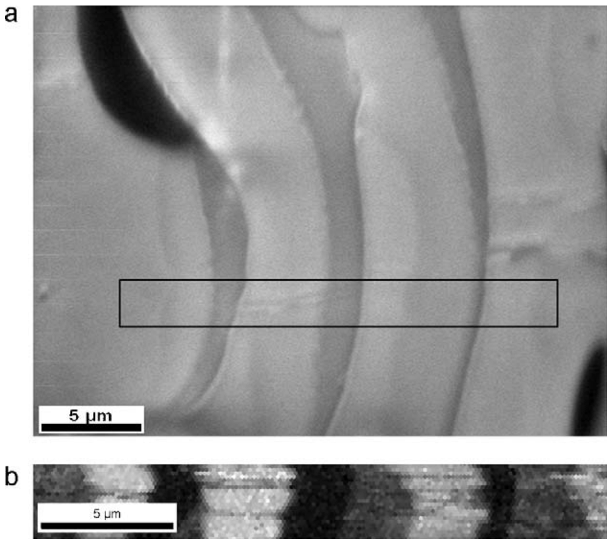

Fig. 5. Scanned area (a) and EBSP-quality mapping (b) of three amorphous sub-lamellae in a cross section of sample 80:10:10.

Table 4
Results of area fraction of amorphous sub-lamellae from image analysis.

Sample	Area fraction of amorphous sub-lamellae (%)
100:00:00	5
90:00:10	20
90:10:00	25
90:05:05	10
85:05:10	15
85:10:05	10
80:10:10	20

3.2. Rietveld analysis

The results of the Rietveld analysis are shown in Table 5. A clear mis-estimation of the phase fractions appear, the measured ZnO-fraction should be higher than the added amount of 20 wt.% due to the presence of an amorphous content. The calculations for the amorphous content determination were adopted from Westphal et al. [40]. Only the final formula (1) including a correction factor will be presented here, for its derivation please see the above mentioned publication.

$$A = \frac{100\%}{100\% - R} \cdot 100\% \cdot \left(1 - \frac{R}{C \cdot R_R}\right) \tag{1}$$

A, amorphous content in the sample; R, amount of added standard; C, correction factor; R_R, amount of standard calculated with Rietveld analysis.

The clear trend of a systematic underestimation of the ZnO content in the 7 samples justifies the application of a correction factor. The expected weight fraction of ZnO from Rietveld analysis in the sample 100:0:0 with an amorphous content of 5% was calculated and the ratio of that expected value to the measured value was considered as the correction factor for all samples. The assumed 5% amorphous content in the sample 100:0:0 was derived from the image analysis presented previously. The measured and corrected weight fractions are presented in Table 5 and, for better comparability and recognizeability, in Fig. 6. Assuming an uncertainty of 1% for the Rietveld method itself the uncertainty range for the amorphous content calculated by formula (1) is presented in Fig. 7. The 1% uncertainty of the Rietveld analysis determines the accuracy of the correction factor C and the amount of standard calculated with Rietveld analysis R_R. This uncertainty decreases with increasing amorphous content and represents a total value. However, the relative differences between each composition can be regarded to with much higher reliability, because the error is similar for each composition due to identical analysis strategy and procedure. Ti^{4+} and Zr^{4+} are incorporated up to a certain degree into the γ-Al_2O_3 lattice; Zr^{4+} has hereby a bigger influence on the lattice parameter due to its higher ionic radius compared to Ti^{4+} (Fig. 8). Therefore ZrO_2 addition should show a stronger influence on the

Table 5
Results of Rietveld analysis and corrected weight fractions excluding standard for the crystalline and amorphous phases.

Sample	Phases	Weight fractions from Rietveld analysis (wt.%)	R-value of each phase (%)	R-value profile (%)	Corrected weight fractions for crystalline and amorphous phases (wt.%)
100:00:00	ZnO	13.5	3.55	9.82	–
	γ-Al_2O_3	85.3	13.27		93.8
	α-Al_2O_3	1.1	37.36		1.2
	Amorph	–	–		5.0
90:00:10	ZnO	19.1	4.72	6.62	–
	γ-Al_2O_3	80.2	12.92		59.3
	t-ZrO_2	0.7	46.49		0.5
	Amorph	–	–		40.2
90:10:00	ZnO	16.1	3.00	11.54	–
	γ-Al_2O_3	83.9	33.34		75.6
	Amorph	–	–		24.4
90:05:05	ZnO	15.2	3.34	8.84	–
	γ-Al_2O_3	83.7	22.62		80.5
	$Zr_5Ti_7O_{24}$	1.1	92.00		1.0
	Amorph	–	–		18.5
85:05:10	ZnO	21.1	6.28	6.63	–
	γ-Al_2O_3	77.3	19.02		50.8
	$Zr_5Ti_7O_{24}$	1.5	86.93		0.9
	Amorph	–	–		48.3
85:10:05	ZnO	19.2	7.58	9.08	–
	γ-Al_2O_3	80.8	31.62		59.4
	Amorph	–	–		40.6
80:10:10	ZnO	23.0	9.30	6.18	–
	γ-Al_2O_3	73.4	18.30		43.3
	$Zr_5Ti_7O_{24}$	3.6	60.51		2.1
	Amorph	–	–		54.6

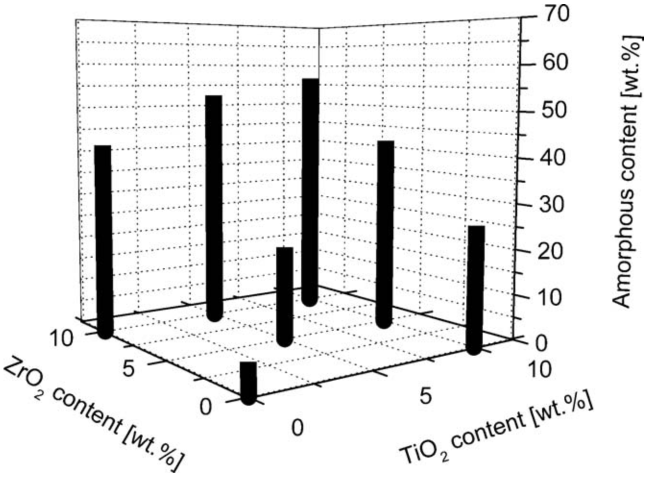

Fig. 6. Total amorphous content by Rietveld analysis.

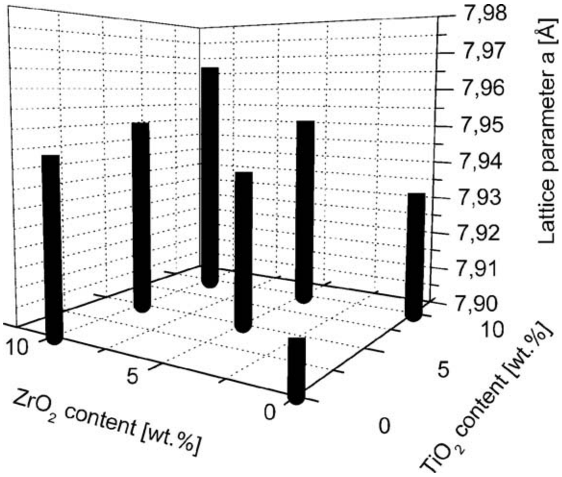

Fig. 8. Lattice parameter of γ-Al_2O_3 as a function of additions.

amorphous content due to its lower degree of fitting into the γ-Al_2O_3 lattice (compare Figs. 6 and 8) [33].

There are clear differences between the areas and, in a first approximation, the weight percentage of the amorphous sub-lamellae and the amorphous amount derived from X-ray diffraction. This gap seems connected with either the binary composition alumina–zirconia or the ternary compositions. This gap additionally becomes bigger with increasing amount of additions in the ternary compositions. This can be explained by the occurrence of secondary amorphous areas that in contrast to the amorphous sub-lamellae are distributed over the sample. To investigate this assumption transmission electron microscopy was applied to the sample 80:10:10. This sample shows a high amount of secondary amorphous content that should simplify the finding of these areas in TEM-examinations.

3.3. TEM investigation

The three different areas distinct with electron diffraction (see Fig. 5) could also be found in TEM investigations. The boundaries between these regions of distinct crystallinity are quite sharp (Figs. 9 and 10), the transition between mixed and only crystalline areas can be seen in the left top corner of Fig. 10. Therefore it can be deduced, that there is clearly a mixed crystalline and amorphous area, the crystallites can be seen by different contrasts and the amorphous state is indicated by the absence of any diffraction pattern (Fig. 11). A detailed view of a secondary amorphous zone is presented in Fig. 12. The secondary amorphous zones are aligned parallel with the dendritic grown crystallites. They exhibit a diameter of 50 nm and a length of several 100 nm. The composition of the dendrites and the secondary amorphous zones was determined with EDX analysis. The dendrites show a composition similar to the starting material. The secondary amorphous zones show about 90 wt.% Al_2O_3 and a TiO_2:ZrO_2 ratio of 2:1. The crystallites in the only crystalline zone are bigger than those in the dendritic zones and show a globular shape. The size of the crystallites in the mixed zone is in the range of the diameter of the electron beam used for electron diffraction and explains thus the

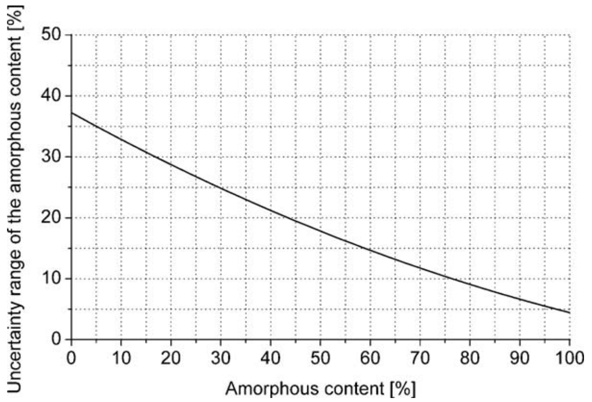

Fig. 7. Uncertainty range from Rietveld analysis assuming 1% accuracy.

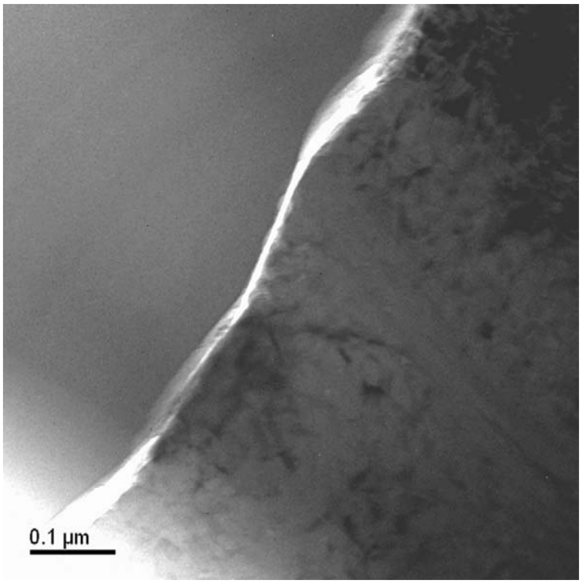

Fig. 9. Transition between primary amorphous and mixed area in 80:10:10.

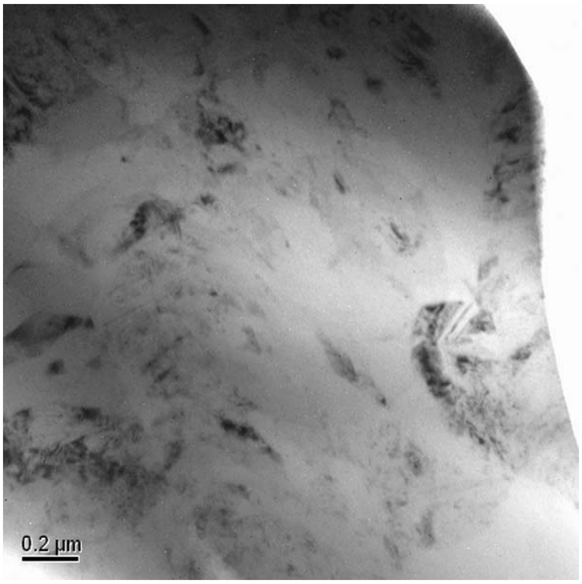

Fig. 10. Transition from mixed to crystalline area in 80:10:10.

poor quality of the diffraction patterns found. The amorphous phase has lower hardness than the crystalline phases, resulting in a stronger removal of these zones during sample preparation and polishing. This prevents gaining useful results from EDX-mapping of the mixed areas, because the rate of X-ray quantum generation is here dependent on the sample thickness.

4. Discussion

The primary amorphous regions are induced by rapid cooling. Such contrasted areas (compare micrographs of amorphous sub-lamellae in section ‘‘3.1 Electron microscopy and electron diffraction’’, Figs. 1–5) in the systems Al_2O_3, TiO_2 and HA can also be seen in micrographs presented in Refs. [41–48], but there is either no discussion of their origin or their potential amorphous nature. In the opinion of the author the absence of a discussion of amorphous sub-lamellae in alumina-based or other oxide materials has several reasons. One might be that the most common thermal spray techniques as plasma spraying or high velocity oxy-fuel spraying involve powders as feed material. This leads to potential contrasts between amorphous and crystalline zones of the microstructure being covered by contrast of lamellae with different chemical compositions due to very little homogenization of powder components during the process. Other reason might be that in pure alumina the amorphous sub-lamellae are very small and might be overseen or even do not appear at all because the applied spray parameter might lead to lower particle or higher substrate temperature. In oxide mixtures the formation of amorphous contents also depends on the degree of mixing and homogenization, so the tendency to form amorphous phase is lower compared with similar materials sprayed with the rod flame spraying technique.

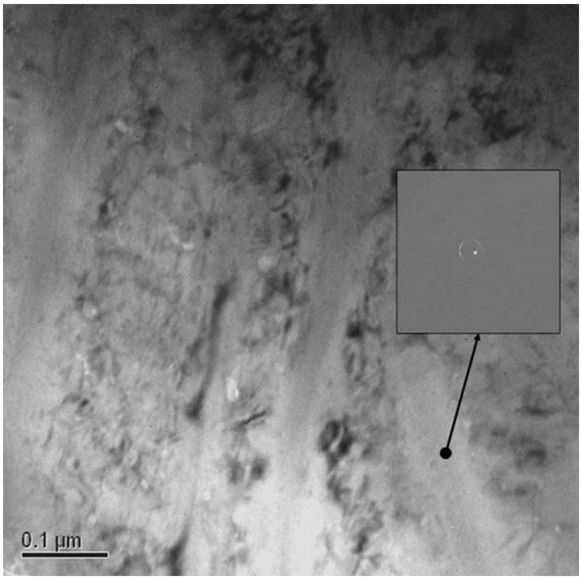

Fig. 11. Mixed amorphous crystalline area with diffraction pattern of secondary amorphous zone in 80:10:10.

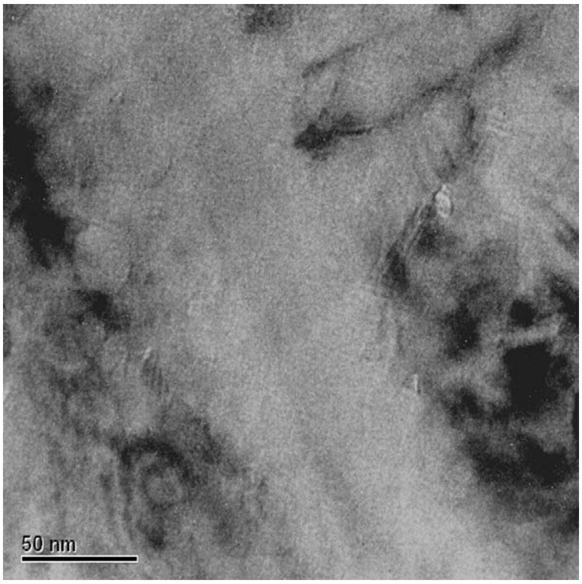

Fig. 12. Detail of secondary amorphous zone in 80:10:10.

What process can lead to the formation of secondary amorphous zones? The depletion of the additions in these secondary zones indicates that demixing, nucleation and crystal growth processes might be involved. Another indication is the fact, that TiO_2 and ZrO_2 are often used as nucleation agents in oxide systems [33,49]. In the glass–ceramic system keatite mixed crystal $ZrTiO_4$ is formed in the presence of TiO_2 and ZrO_2 [50]. Thus an influence by the nucleation of ZrO_2 or various Zirkoniumtitanates respectively in this ternary system is very likely to appear [34,51,52]. The effect of spinodal demixing might provide embryonic crystals inducing nucleation during the rapid cooling. According to Hudon and Baker [53] spinodal demixing appears in binary silicate systems, if the following criteria are fulfilled: First, the bond strength of the network former ion with the oxygen ion is within the range of 0.26–0.83 kJ/mol; second, the coordination number of the network modifier ion is different to one of the network former; and third, the field strength of the cations according to Dietzel is in the range -0.02 to 0.06 and 0.8–0.9. All these criteria are met in this ternary system making the occurrence of spinodal demixing very likely. For the primary amorphous area the cooling speed is high enough to prevent spinodal demixing. In the system Al_2O_3–SiO_2 this critical cooling rate is between 10^5 and 10^7 K/s [53], laying within the range occurring during droplet impact of thermally sprayed materials [54]. If the cooling speed drops with increasing thickness of the solidified lamella due to decreasing heat flow and release of solidification enthalpy, spinodal demixing can appear leading to homogeneous nucleation and growth of ZrO_2 or $Zr_5Ti_7O_{24}$ and heterogeneous nucleation of γ-Al_2O_3. If the growth rate of the ZrO_2 or $Zr_5Ti_7O_{24}$ is much higher than that of γ-Al_2O_3, a depleting of TiO_2 and ZrO_2 in the remaining melt appears. If than the concentration of this species drops below a certain limit, the melt moves out of the immiscibility dome and no more spinodal demixing can take place. But the cooling speed is still high enough to lead to amorphous phase. The composition of the secondary amorphous zones gives the compositional limit of spinodal demixing. It seems that Zr^{4+} has a stronger effect than Ti^{4+} what can be traced to the higher difference in coordination number with Al^{3+} for Zr^{4+} compared to Ti^{4+}.

5. Conclusion

Two distinct amorphous zones appear in flame sprayed Al_2O_3–TiO_2–ZrO_2 coatings; first, due to rapid cooling in a glass-like system and second, most probably due to spinodal demixing induced nucleation and growth effects. This model provides an explanation for the observed distribution and for the tendencies of the total and the distinct amounts of the amorphous contents as a function of amount and kind of TiO_2- and ZrO_2-addition.

Acknowledgements

The authors would like to thank Dr. Berek for conducting electron diffraction experiments and Dr. Klemm for transmission electron microscopy.

References

[1] H.J. Kim, Y.J. Kim, Amorphous phase formation of the pseudo-binary Al_2O_3–ZrO_2 alloy during plasma spray processing, Journal of Materials Science 34 (1999) 29–33.

[2] J. Suffner, H. Sieger, H. Hahn, S. Dosta, I.G. Cano, J.M. Guilemany, P. Klimczyk, L. Jaworska, Microstructure and mechanical properties of near-eutectic ZrO_2–60 wt.% Al_2O_3 produced by quenched plasma spraying, Materials Science and Engineering A 506 (2009) 180–186.

[3] J. Suffner, H. Hahn, S. Dosta, I.G. Cano, J.M. Guilemany, Influence of liquid nitrogen quenching on the evolution of metastable phases during plasma spraying of (ZrO_2–5 wt.% Y_2O_3)–20 wt.% Al_2O_3 coatings, Surface and Coatings Technology 204 (2009) 149–156.

[4] M.L. Gualtieri, M. Prudenziati, A.F. Gualtieri, Quantitative determination of the amorphous phase in plasma sprayed alumina coatings using the Rietveld method, Surface and Coatings Technology 201 (2006) 2984–2989.

[5] J.D. Haman, K.K. Chittur, D.E. Crawmer, L.C. Lucas, Analytical and mechanical testing of high velocity oxy-fuel thermal sprayed and plasma sprayed calcium phosphate coatings, Journal of Biomedical Materials Research 48 (1999) 856–860.

[6] Y.C. Tsui, C. Doyle, T.W. Clyne, Plasma sprayed hydroxyapatite coatings on titanium substrates. Part 1: mechanical properties and residual stress levels, Biomaterials 19 (1998) 2015–2029.

[7] X. Zhou, V. Shukla, W.R. Cannon, B.H. Kear, Metastable phase formation in plasma-sprayed ZrO_2 (Y_2O_3)–Al_2O_3, Journal of the American Ceramic Society 86 (2003) 1415–1420.

[8] A. Pawlowski, J. Morgiel, T. Czeppe, Amorphisation and crystallisation of phases in plasma sprayed Al_2O_3 and ZrO_2 based ceramics, Archives of Metallurgy and Materials 52 (2007) 635–639.

[9] Y. Li, K.A. Khor, Mechanical properties of the plasma-sprayed Al_2O_3/$ZrSiO_4$ coatings, Surface and Coatings Technology 150 (2002) 143–150.

[10] D.T. Weaver, D.C. Van Aken, J.D. Smith, The role of bulk nucleation in the formation of crystalline cordierite coatings produced by air plasma spraying, Materials Science and Engineering A 339 (2003) 96–102.

[11] B.H. Kear, Z. Kalman, R.K. Sadangi, G. Skandan, J. Colaizzi, W.E. Mayo, Plasma-sprayed nanostructured Al_2O_3/TiO_2 powders and coatings, Journal of Thermal Spray Technology (2000) 9.

[12] Y. Yuanzheng, L. Zhiguo, L. Zhengyi, C. Yuzhi, Interfacial phenomena in the plasma spraying Al_2O_3 + 13 wt.% TiO_2 ceramic coating, Thin Solid Films 388 (2001) 208–212.

[13] D. Zois, A. Lekatou, M. Vardavoulias, A microstructure and mechanical property investigation on thermally sprayed nanostructured ceramic coatings before and after a sintering treatment, Surface and Coatings Technology 204 (2009) 15–27.

[14] K. Gross, W. Walsh, E. Swarts, Analysis of retrieved hydroxyapatite-coated hip prostheses, Journal of Thermal Spray Technology 13 (2004) 190–199.

[15] S. Beauvais, V. Guipont, F. Borit, M. Jeandin, M. Español, K.A. Khor, A. Robisson, R. Saenger, Process–microstructure–property relationships in controlled atmosphere plasma spraying of ceramics, Surface and Coatings Technology 183 (2004) 204–211.

[16] K.A. Gross, C.C. Berndt, H. Herman, Amorphous phase formation in plasma-sprayed hydroxyapatite coatings, Journal of Biomedical Materials Research 39 (1998) 407–414.

[17] T. Chráska, J. Hostomský, M. Klementová, J. Dubský, Crystallization kinetics of amorphous alumina–zirconia–silica ceramics, Journal of the European Ceramic Society 29 (2009) 3159–3165.

[18] T. Chraska, K. Neufuss, J. Dubsky, P. Ctibor, M. Klementova, Fabrication of bulk nanocrystalline ceramic materials, Journal of Thermal Spray Technology 17 (2008) 872–877.

[19] A.L. Vasiliev, N.P. Padture, X. Ma, Coatings of metastable ceramics deposited by solution-precursor plasma spray: I. Binary ZrO_2–Al_2O_3 system, Acta Materialia 54 (2006) 4913–4920.

[20] A.L. Vasiliev, N.P. Padture, Coatings of metastable ceramics deposited by solution-precursor plasma spray: II. Ternary ZrO_2–Y_2O_3–Al_2O_3 system, Acta Materialia 54 (2006) 4921–4928.

[21] L.L. Shaw, D. Goberman, R. Ren, M. Gell, S. Jiang, Y. Wang, T.D. Xiao, P.R. Strutt, The dependency of microstructure and properties of nanostructured coatings on plasma spray conditions, Surface and Coatings Technology 130 (2000) 1–8.

[22] H.C. Chen, J. Heberlein, E. Pfender, TEM characterization of plasma-sprayed thermal barrier coatings and ceramic–metal interfaces after hot isostatic pressing, Thin Solid Films 301 (1997) 105–114.

[23] W. Braue, G. Paul, R. Pleger, H. Schneider, J. Decker, In-plane microstructure of plasma-sprayed Mg–Al spinel and 2/1-mullite based protective coatings: an electron microscopy study, Journal of the European Ceramic Society 16 (1996) 85–97.

[24] Z. Zhize, J. Yuansheng, Tribological and microstructure analysis of three ZrO_2 + Al_2O_3 plasma sprayed coatings, in: ITSC 95 Kobe, High Temperature Society of Japan, Osaka, Japan, 1995, pp. 525–530.

[25] J. Llorca, V.M. Orera, Directionally solidified eutectic ceramic oxides, Progress in Materials Science 51 (2006) 711–809.

[26] N. Claussen, G. Lindemann, G. Petzow, Rapid solidification in the Al_2O_3–ZrO_2 system, Ceramics International 9 (1983) 83–86.

[27] S. Balasubramanian, H. Keshavan, W.R. Cannon, Sinter forging of rapidly quenched eutectic Al_2O_3–ZrO_2(Y_2O_3)-glass powders, Journal of the European Ceramic Society 25 (2005) 1359–1364.

[28] V. Jayaram, C.G. Levi, T. Whitney, R. Mehrabian, Characterization of Al_2O_3–ZrO_2 powders produced by electrohydrodynamic atomization, Materials Science and Engineering A 124 (1990) 65–81.

[29] G. Kalonji, J. McKittrick, L.W. Hobbs, Applications of rapid solidification theory and practice to alumina–zirconia ceramics, Advances in Ceramics 12 (1984) 816–825.

[30] G.N. Greaves, S. Sen, Inorganic glasses, glass-forming liquids and amorphizing solids, Advances in Physics 56 (2007) 1–166.

[31] K.-H. Sun, Fundamental condition of glass formation, Journal of the American Ceramic Society 30 (1947) 277–281.

[32] V.V. Hoang, N.H. Hung, Temperature-induced phase transition in simulated amorphous Al_2O_3, Physica Status Solidi B 243 (2006) 416–423.

[33] H. Scholze, H. Salmang (Eds.), Keramik, Springer, Berlin/Heidelberg/New York, 2007.

[34] D. Caferra, A. Grassi, S. Saiello, A. Buri, A. Marotta, The role of TiO_2 and ZrO_2 in Na_2O–MO_2–SiO_2 glasses, Materials Letters 2 (1983) 53–55.

[35] B. Vessal, C.R.A. Catlow, Amorphous solids, in: Computer Modeling in Inorganic, Crystallography, Academic Press, London, 1997, pp. 295–332.

[36] V.V. Hoang, Structural properties of simulated liquid and amorphous TiO_2, Physica Status Solidi B 244 (2007) 1280–1287.

[37] D. Vanderbilt, X. Zhao, D. Ceresoli, Structural and dielectric properties of crystalline and amorphous ZrO_2, Thin Solid Films 486 (2005) 125–128.

[38] T. Kratschmer, P. Gehre, C.G. Aneziris, Flame spraying of alumina with titania and zircinia additions, in: P. Quirmbach (Ed.), 51st International Colloquium on Refractories, vol. 51, Forschungsgemeinschaft Feuerfest e. V., Aachen, Bonn, Germany, (2008), pp. 24–27.

[39] C.G. Aneziris, P. Gehre, T. Kratschmer, H. Berek, Thermal shock behavior of flame-sprayed free-standing coatings based on Al_2O_3 with TiO_2- and ZrO_2-additions, International Journal of Applied Ceramic Technology (2010) (published online).

[40] T. Westphal, T. Fullmann, H. Pollmann, Rietveld quantification of amorphous portions with an internal standard – mathematical consequences of the experimental approach, Powder Diffraction 24 (2009) 239–243.

[41] E. Turunen, J. Keskinen, O. Heczko, P. Lintunen, T. Gustafsson, Y. Ge, M. Arponen, S.-P. Hannula, Development of nano-reinforced HVOF sprayed ceramic coatings, Advanced Engineering Materials 8 (2006) 669–673.

[42] R.S. Lima, B.R. Marple, Thermal spray coatings engineered from nanostructured ceramic agglomerated powders for structural, thermal barrier and biomedical applications: a review, Journal of Thermal Spray Technology 16 (1) (2007) 40–63.

[43] P. Ctibor, P. Bohác, M. Stranyánek, R. Ctvrtlík, Structure and mechanical properties of plasma sprayed coatings of titania and alumina, Journal of the European Ceramic Society 26 (2006) 3509–3514.

[44] G. Bolelli, V. Cannillo, L. Lusvarghi, T. Manfredini, C. Siligardi, C. Bartuli, A. Loreto, T. Valente, Plasma-sprayed glass–ceramic coatings on ceramic tiles: microstructure, chemical resistance and mechanical properties, Journal of the European Ceramic Society 25 (2005) 1835–1853.

[45] R Tomaszek, L. Pawlowski, J. Zdanowski, J. Grimblot, J. Laureyns, Microstructural transformations of TiO_2, $Al_2O_3 + 13TiO_2$ and $Al_2O_3 + 40TiO_2$ at plasma spraying and laser engraving, Surface and Coatings Technology 185 (2004) 137–149.

[46] X. Lin, Y. Zeng, S.W. Lee, C. Ding, Characterization of alumina–3 wt.% titania coating prepared by plasma spraying of nanostructured powders, Journal of the European Ceramic Society 24 (2004) 627–634.

[47] H. Li, K.A. Khor, R. Kumar, P. Cheang, Characterization of hydroxyapatite/nano-zirconia composite coatings deposited by high velocity oxy-fuel (HVOF) spray process, Surface and Coatings Technology 182 (2004) 227–236.

[48] N.N. Ault, C. Norton, Characteristics of refractory oxide coatings produced by flame-spraying, Journal of the American Ceramic Society 40 (1957) 69–74.

[49] S. Kemethmüller, A. Roosen, F. Goetz-Neunhoeffer, J. Neubauer, Quantitative analysis of crystalline and amorphous phases in glass ceramic composites like LTCC by the Rietveld method, Journal of the American Ceramic Society 89 (2006) 2632–2637.

[50] C.H.-G. Roos, Untersuchungen zum Thermoschockverhalten von Keatit-Mischkristall-Glaskeramiken, Bayerischen Julius-Maximilians-Universität, Dr. -Ing. Würzburg, 2002.

[51] Y.P. Udalov, D.V. Grishchenko, Y.B. Petrov, I.V. Poznyak, A.Y. Pechenkov, Monotectic crystallization of melts in the ZrO_2–Al_2O_3 system, Glass Physics and Chemistry 32 (2006) 479–485.

[52] T. Takamori, R. Roy, Rapid crystallization of SiO_2–Al_2O_3 glasses, Journal of the American Ceramic Society 56 (1973) 639–644.

[53] P. Hudon, D.R. Baker, The nature of phase separation in binary oxide melts and glasses. I. Silicate systems, Journal of Non-Crystalline Solids 303 (2002) 299–345.

[54] R. McPherson, On the formation of thermally sprayed alumina coatings, Journal of Materials Science 15 (1980) 3141–3149.